Laminar buffet and flow control

Vincent Brion, Julien Dandois, Rouven Mayer, Philippe Reijasse, Thorsten Lutz, Laurent Jacquin

Laminar buffet and flow control

V. Brion*, J. Dandois*, R. Mayer**, P. Reijasse*, T. Lutz**, L. Jacquin*

*vincent.brion@onera.fr, ONERA, The French Aerospace Lab

** USTUTT, University of Stuttgart

Abstract

An experimental investigation of the transonic flow past the laminar OALT25 airfoil has been conducted to analyze the impact of laminar flow upon the shock wave dynamics and the existence of a laminar buffet like phenomenon. Tests have been carried out at freestream Mach numbers varying in the range 0.7 to 0.8, angle of attack from 0.5 to 4 degrees and with two tripping configurations at the upper surface of the wing. The (airfoil) chord based Reynolds number is about 3 millions. Results obtained from pressure taps and sensors measurements, as well as Schlieren visualizations of the flow reveal the presence of a laminar buffet phenomenon in sharp contrast with the turbulent phenomenon, as it features a (freestream and chord) based normalized frequency of about unity while turbulent buffet occurs for a frequency close to 0.07 (Jacquin et al., AIAA Journal, vol. 47, number 9, 2009). A low frequency mode, at a frequency about 0.05 is also present in the laminar situation, notably lower than the high frequency component. The latter exhibits strong oscillations of the shock foot and vertical wavelike deformations of the shock wave and the former moves the shock back and forth over a small portion of chord, quite similarly to the turbulent phenomenon. The mean flow past the laminar wing is characterized by a laminar separation bubble under the shock foot which likely contributes much to the novel dynamics revealed by the present experiments. Two control strategies of the unsteady shock wave are implemented, one consisting of three-dimensional bumps and one consisting of steady jets blowing transversely to the freestream. It is found that bumps provide a significant reduction of the buffet intensity in the laminar situation. The jets are able to completely remove the flow unsteadiness in both laminar and turbulent conditions.

1 Introduction

Transonic buffet is one of the limitations of the flight envelope of commercial aircrafts. It also limits the performance of military aircrafts engaged in air-to-air combat at high subsonic speeds due to the development of flow separation on the wing and oscillations of the shock wave which may cause the buffeting of the airframe and steep increases in drag (Ray and Taylor [36]). For civilian aircraft certification authorities buffet onset boundaries is based on accelerometer recordings at the position of the pilot's seat with peak to peak amplitudes of 0.25 acceleration of gravity (g) (Obert [34]). Buffet onset is therefore an important feature to be determined in the development of a wing configuration as it dictates the necessary margin to critical conditions and aircraft certification. Mabey [29] and Ray and Taylor [36] used the data of a strain gage installed at the root of an elastically similar wing to determine the oscillations of the wing structure in response to the energy provided by shock oscillation and flow separation. In this process they could describe the onset of buffet. However using similarity for the wing elastic response is a difficult task and pure aerodynamical studies of the buffet, with ideally rigid wing, is a much easier way to go. In this case, criteria based on selected divergences in the static aerodynamic characteristics allow a qualitative determination of the buffet onset (see John [23]).

At a fundamental level, much understanding of the buffet phenomenon has been obtained from experiments of the transonic flow past simple airfoils. In this case it is known that starting from a stable configuration an increase in Mach number or angle of attack eventually causes the de-

velopment of large oscillations of the shock wave that forms at the end of the supersonic pocket above the upper surface of the profile. This two-dimensional buffet phenomenon has been much described in experiments (see Jacquin et al. [22], McDevitt [31] and Lee [27]) and has recently been shown to correspond to the nonlinear saturation of a global unstable mode by Crouch et al. [12] and Sartor et al. [38]. Earlier Lee [26] proposed an acoustic feedback loop scenario to explain the buffet phenomenon, that comprises hydrodynamic waves travelling from the shock to the trailing edge, where acoustic waves are emitted. These acoustic waves travel upstream and reach the shock back, triggering new hydrodynamic perturbations at the shock foot. This mechanism was also considered by Jacquin et al. [22] and recent Particle Image Velocimetry (PIV) tend to confirm this scenario, see Hartmann et al. [21, 20]. Numerical simulations using RANS models and hybrid RANS-LES models have also successfully been used to simulated buffet for various airfoils [15, 5, 44, 4, 6]. Compared to the two-dimensional phenomenon, the three-dimensional buffet on typical aircraft wing geometries appears quite different. It implies much less shock oscillations and a wider spectral content of fluctuations (see Dandois [13] and Sartor and Timme [39]).

These previous studies were concerned with the shock interaction with a turbulent boundary layer, meaning, from an experimental point of view at least, that the boundary layer that forms at the upper surface of the wing is tripped turbulent at some location close to the leading edge. The case of an interaction with a laminar boundary layer has been comparatively much less investigated. The experimental analysis of Dor et al. [16], one of the few references in this domain, suggests the absence of a marked unsteadiness in the laminar, free transition, case. On the contrary Finke [18] mentions, based on transonic experiments past the $\mathrm{NACA63}_1 - 012$ airfoil, the existence of a high frequency mode at normalized frequency (based on free stream and chord) $S_t \simeq 0.2 - 0.4$ at low angle of attack and of a low frequency mode $S_t \simeq 0.08$ at higher angles of attack. The low frequency mode is associated with a large extension of the shock movement, similar to the turbulent buffet phenomenon and unlike the high frequency mode which negligeably moves the shock. Finke further analyzes the high frequency mode as the result of a loop of excitations that proceeds within the laminar separation bubble present under the shock foot in the laminar case. This loop seemingly develops between the separation point and the reattachment point where pressure waves are emitted, then propagating upstream. The low frequency mode is analyzed similarly to the acoustic feedback loop scenario which was made popular by Lee [26]. The work of Finke, recently summarized by Soda [43], also contains models based on these scenari that match experimental results rather well. Finally, at a more general level, Liepmann [28] stresses the importance of boundary layer effects upon the shock wave phenomenon using experimental investigations of the flow past a circular airfoil.

From the numerical side little work has been done on the influence of laminar flow on buffet. There is, on general grounds, some numerical difficulty to model and capture the transitional state of the boundary layer, to account for the coupling with the external shocked flow, and to deal with the flow unsteadiness. In Reyhner and Flugge-Lotz [37] the problem of the interaction is treated by fixing the positions of the start of the interaction and of an idealized shock wave then using an iterative procedure to ensure the compatibility of the shock strength with these positions. However the entire flow remains laminar. Reynolds Average Navier Stokes (RANS) approaches implement transition criteria to account for varying boundary layer states, that range from practical to stability based theoretical approaches. However recent simulations performed in the framework of the Buterfli project led by Europe and Russia on this specific issue, this program being the one that funded the current wind tunnel tests, showed the limitations of current numerical methods (see one of the summary report of the project results [1]). These were found to fail in providing or even converging a realistic average flow field when reaching critical conditions. As a consequence one needs to use Direct Numerical Simulation (DNS) or Large Eddy Simulation (LES) to calculate the situation, although at a high computational cost and with little possibilities to carry out the parametric study necessary to improve current understanding. Recently Dandois et

al. [14] exposed a Large Eddy Simulation (LES) reproduction of the present experiment, implicitly taking advantage of the strong shock at the upper surface of the airfoil to trigger the transition, and letting the numerical scheme accounting for the details of the small scale fluctuations.

The present experimental analysis aims at describing this flow behavior associated with free transition. A transonic airfoil with a laminar design is considered and wind tunnel tests are performed. Following the previous tests performed on this setup by the same authors (Brion et al. [8]), it is known that the laminar separation bubble that forms under the shock foot in the laminar case is a key changer of the dynamics compared to the turbulent case. The presence of this laminar separation in the shock interaction under buffet condition was first mentionned by Finke [18]. From a general perspective, it is well known that laminar flow upstream is more sensitive to adverse pressure gradient. In the case of a laminar boundary layer interacting with a normal shock wave typical of the transonic flow past an airfoil flow separation can not be avoided (Schlichting [40]) and occurs at some distance, named the interaction length, upstream of the shock wave. The resulting laminar recirculation bubble tends to hasten the developement of turbulence as shear instabilities (Kelvin-Helmholtz) generate strong amplification of upstream perturbations, as illustrated in the incompressible case by Jones et al. [24]. As a consequence the flow downstream of the interaction is generally turbulent. The recirculating flow inside the laminar separation can also favors feedback from the reattachment to the separation points. The latter, which is highly sensitive to disturbances, causes additional perturbations to the laminar bubble. Due to the strong amplification produced by the Kelvin-Helmholtz instability, the complete process can become unstable, as proposed by Finke [18] to explain the high frequency dynamics of the laminar interaction. Finally Reyhner and Flugge-Lotz [37] and Babinski and Harvey [3] describe how a laminar interaction creates a two stage pressure increase in the shock region, one from the compression waves formed at the flow separation upstream from the shock wave and one from the very shock wave. The resulting pattern is typical of the laminar interaction.

The improvement of numerical codes to capture the flow dynamics in a such transitional configurations relies on the availability of experimental data to confront the outputs of models or motivate their development. One concern is about the setup of transition criteria capable of unsteadiness, as this does not seem to have ever been developped so far. The data obtained in the current study could provide reference data in this domain, with variations in Mach number, angle of attack, and considering both turbulent and laminar boundary layer configurations upstream of the shock wave.

It will be shown from the experimental results that unlike the description of Dor et al. [16] and similarly to the analysis of Finke [18] an unsteady phenomenon also exists in the laminar case above critical conditions, at a rather high frequency compared to turbulent buffet. The existence of this phenomenon was reported in a previous article (Brion et al. [8]) and the present article provides additional details on the flow dynamics, in particular the existence of a low frequency peak similar to the turbulent buffet, which was also mentioned by Finke [18]. Another goal of the present study is to investigate the possibility to reduce or postpone buffet. Flow control for wing operation is useful to increase flight envelope and maneuverability. Delaying buffet can extend the upper limit of the flight enveloppe. As such it has been attempted in several occasions. Cornettte [11] identified a reduction in turbulent buffet intensity and an increased margin to buffet onset when using special bodies for reduced shock-induced separation, one of the basic phenomenon correlated with buffet onset. In a three-dimensional turbulent configuration Molton et al. [33] showed that mechanical, continuous, and pulsed fluidic vortex generators were capable of postponing buffet onset in a three-dimensional buffet half wing configuration, through the reduction of flow separation behind the shoch wave.

This paper first describes the experimental setup that is deployed to investigate the flow dynamics in laminar conditions, taking the turbulent flow case as a preliminary validation of the experimental method and then as a reference for the rest of the analysis. The second part deals with the analysis of the experimental database, that comprises time averaged and fluctuations of

pressure at the wing surface, Schlieren visualizations and observations of the laminar separation bubble with water droplets obtained by naturally condensing the water vapor present in the air of the wind tunnel. The last section is devoted to the control of the flow using two techniques, three-dimensional bumps and steady jets, considering the turbulent and laminar cases.

2 Description of the experiment

2.1 Wind tunnel setup

The experimental setup is an airfoil installed horizontally in the test section of the S3Ch transonic wind tunnel at the ONERA Meudon research center. The test section is 2.2m long, 0.763m in height and 0.804m in width. The Mach number in the test section can be varied from 0.3 to 1.2 and is used here in the high subsonic range 0.7-0.8. In this range the Mach number is set using a second throat located downstream of the test section. The use of this second throat ensures an independence of the flow in the test section with regards to perturbations generated in the diffusor and allows to stabilize the Mach number to ± 0.001. Stagnation pressure in the settling chamber is equalized to atmospheric conditions ahead of the last turbulence wire mesh. Automatic temperature controls maintain a uniform and constant stagnation temperature of 316K. The dewpoint is controlled in order to prevent condensation in the test section, unless otherwise stated.

The airfoil features the OALT25 design, an ONERA shape targetted for improved laminar flow, that is close to OAT15A design previously used to investigated the buffet phenomenon in a turbulent situation, see Jacquin et al. [22]. The airfoil is displayed in figure 2 in dimensionless units. Here the chord of the wing is $c = 0.23m$ and the freestream velocity U_0 are considered for normalization. The Reynolds number is approximately 3×10^6. The angle of attack of the airfoil can be varied from 0 to 4 degrees. The freestream dynamic pressure is noted q_0 and equals $\frac{1}{2}\rho U^2$. Time is normalized on $\frac{c}{U_0}$ and frequencies are usually presented in terms of Strouhal number $S_t = \frac{fc}{U_0}$.

Adaptive upper and lower walls allow to counter test section variations due to the presence of the model and boundary layer growth at the side walls so as to minimize Mach number and flow incidence changes in the volume of the wing. At first order, upper and lower walls provide contouring close to the streamlines of the flow past the wing as if it was in free atmospheric conditions. Wall adaptation is performed whenever a setting of the test is changed, that is Mach number, angle of attack or state of the boundary layer at the wing upper surface. Three-dimensional effects are minimized by the large aspect ratio of the wing $\lambda = \frac{s}{c} \simeq 3.5$ where $s = 0.804$ is the wing span, equal to the width of the test section. Moreover there is no support inside the test section to prevent unwanted surface interactions and wake development.

An important flow parameter in the present study is the state of the boundary layer upstream of the shock wave at the suction side. In the free transition case the boundary layer remains laminar up to the shock wave. This is evidenced in figure 1 which shows the upper surface of the wing in the infrared (IR) $2.5 - 5.1\mu m$ light range with the flow coming from the left. The surface temperature shows a steep increase approximately at mid-chord as a result of the compression (and thus external flow temperature increase) associated with the shock wave. An isolated roughness has been installed slightly downstream of the leading edge at a specific spanwise position to illustrate the impact of a turbulent wedge in the IR image. The wedge is easily identified in the image. By contrast, this shows that a laminar state is established in the rest of the wing up to the shock wave. In practice, IR thermography was used to check that the upper surface was free from such unwanted turbulent transition wedge. Indeed any roughness would cause the same visualization as the one in figure 1. No IR monitoring could be applied at the lower surface and thus to ascertain the boundary layer state it was forced turbulent by tripping tape installed at 7% of chord. The tripping tape features a sawtooth design and is taken with a thickness equal to $0.1mm$ when installed at 7% of chord.

To conduct IR monitoring the wing has first been painted with black mast paint of the brand

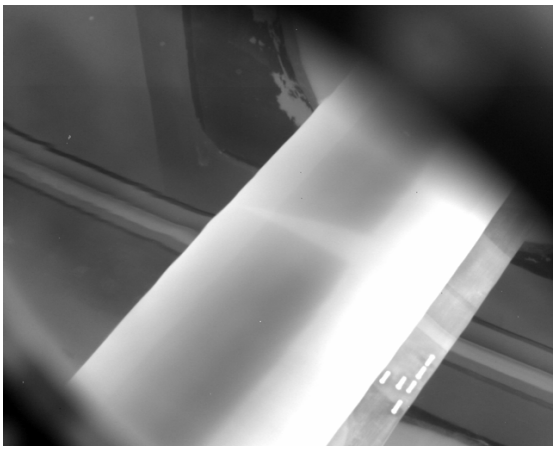

Figure 1: Infrared image of the upper surface of the wing at Mach number 0.73 and angle of attack 2 degrees. The flow comes from the left. An isolated roughness installed at the leading edge creates the turbulent wedge that protrudes ahead of the temperature increase (from dark to white) associated with the shock wave and the rise of turbulence. The wedge semi-angle is about 7^o.

Sacotherm. This increases the emissivity of the surface and improves the contrast of the IR image. Furthermore due to constraints with the optical access the IR imaging has been established through a reflection at the upper wall of the test section, which had been polished beforehand. IR thermography has only been used in the first part of the wind tunnel tests that correspond to the uncontrolled case. In the second part of the tests dedicated to control an unpainted surface was used instead and the laminar quality of the flow was checked using a laminar pattern in the pressure distribution at the upper surface of the airfoil. The possibility to use pressure distribution to check for flow laminarity is explained in the present paper.

An individual test in the present experiment is described by the freestream Mach number, the angle of attack of the wing and the position of the tripping that is installed at the upper surface of the wing. In the following any tests will hence be characterized by the set of parameters (M, α, tr) with M the Mach number, α the angle of attack of the wing and tr the location of the tripping tape on the upper surface in percent of chord from the leading edge. The case $tr = 0$ means free transition, i.e. no tripping is used. Furthermore an indication of the presence of paint (w/) or not (w/o) is given when necessary, as this is shown to play a role in the flow dynamics.

The first diagnostic is performed with a Schlieren visualization of the flow, on the basis of a high-speed recording (Phantom camera) at a frame rate equal to 6006 frame per second (fps), exposure time of $1\mu s$ and 16bits resolution per pixel (px). The size of the sensor is $800px \times 600px$. The intensity of the Schlieren visualisations results from an integration process of the light beams deflected by the variations in refractive index perpendicular to the knive edge that are caused by the flow [42]. For a gas refractive index is linearly related to flow density with the Gladstone-Dale constant [32]. Here the knive is set vertically and the Schlieren images show the field of $I = \frac{\partial \rho}{\partial x}$ that primarily highlights the shock wave and the flow structures that form downstream.

The wing is equipped with pressure taps and sensors, as illustrated in figure 2. Sensors and taps are aligned along two different lines which are inclined about the free stream at an angle larger than 7 degrees (the typical angle of a turbulent wedge, as obtained in the present test, see figure 1) to prevent cross-contamination and early transition to turbulence. For similar reasons the fore part (20%) of the wing is free of any equipment. From 40% of chord, sensors and taps at the upper surface are almost uniformly distributed at a spacing equal to 3-4% of chord. The lower surface is equipped with a few devices.

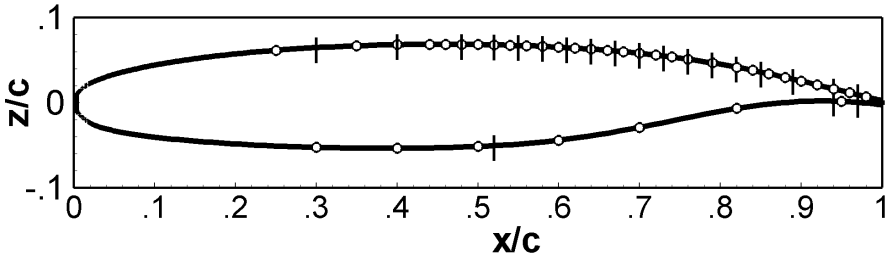

Figure 2: Airfoil design and pressure equipment along the chord. Circles and vertical ticks indicate pressure taps and sensors, respectively.

The description of the experimental tests must be completed with the information on the shape of the adapative upper and lower walls and the value of the turbulence level of the incoming flow. For the former point we present the shape of the adaptive walls, in terms of the vertical displacement Δh_{ts} of the walls about horizontal as a function of longitudinal distance x_{ts}, here normalized on test section height $H = 0.763$ and starting from zero at test section entrance (note that $_{ts}$ refers to *test section*), for the turbulent and laminar configurations in figure 3, for a Mach equal to 0.735 and incidence equal to 4^o. Wall deformations are globally oriented upward as a consequence of the lift generated by the airfoil. In addition the bottom and top walls diverge to account for the blockage of the model, and the top wall exhibits the larger deformation because of the strongest aerodynamic variations that occur at the upper surface of the airfoil compared to the lower surface. The turbulence level of the incoming flow has been measured using a hot-wire probe (model 55R41 by Dantec) at several values of the Mach number. A constant current hot-wire anemometer is used. The hot-wire probe was preliminary calibrated in situ for several value of the Mach number in the transonic regime, yielding a relationship between ρU_0 the longitudinal flow momentum obtained from stagnation conditions and static pressure in the test section and E_{hw} the voltage given by the anemometer. The calibration law includes a correction for the influence of flow temperature (typically $E_{hw} \propto -0.035\Delta T$ where ΔT is the variation in temeperature about some given target value T_0 of the calibration). Table 1 provides the value of the rate of turbulence for the range of Mach number of interest. Note that here the turbulence rate Tu is defined as

$$Tu = \frac{\sqrt{\overline{(\rho u - \overline{\rho u})^2}}}{\overline{\rho u}} \tag{1}$$

to account for the dependence of the hot-wire signal on both variations of flow velocity and specific mass. Note that the overline symbols denotes time averaging. Freestream turbulence can also be given in terms of the N factor for natural transition, that we note here N_{tr}. This parameter can be deduced from the rate of turbulence using the empirical relation given by Mack [30] that is $N_{tr} = -8.43 - 2.4ln(Tu)$ and is also indicated in table 1. The fluctuations of the flow in the test section are reasonably low, and adequate in practice to allow for a laminar boundary layer to develop at the surface of the wing.

2.2 Validation step

The experimental setup is first validated against the fully turbulent case $tr = 7$ case, i.e. when the boundary layer at the upper surface is forced turbulent by the tripping device (sawtooth tape) installed at 7% of chord. The data obtained in this configuration is compared to the one described in the work of Jacquin et al. [22] which is obtained with the supercritical OAT15A airfoil.

Table 1: Turbulence level and associated N factor for transition N_{tr} of the freestream of the wind tunnel for several Mach numbers in the Mach range considered for the present tests.

Mach	**Tu**	$\boldsymbol{N_{tr}}$
0.70	0.0026	5.8
0.75	0.0026	5.8
0.80	0.0020	6.4

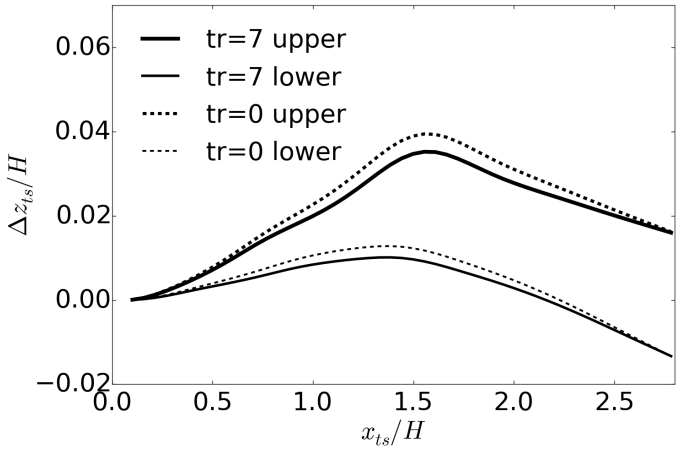

Figure 3: Shape of the upper and lower adaptive walls in the turbulent and laminar cases with $(M, \alpha) = (0.735, 4^o)$. Distances are normalized upon the height of the test section. The origin of the longitudinal distance x_{ts} is the end of the nozzle.

Figure 4 displays pressure spectra in terms of the onesided Power Spectral Density (PSD) $\hat{p}^2$ normalized on q_0^2 for data taken at the trailing edge of the wing ($x/c = 97\%$) and for different Mach numbers and angles of attack. Pressure signal are obtained with a sampling rate of 10240Hz and acquisition time of 40s. PSDs are esimated using the Welch method, blocks of 4096, hanning windowing and 50% overlap, and are scaled by frequency (therefore they are given in units of Hz^{-1}). The existence of critical conditions below which the flow is steady and above which it is unsteady agrees with the descriptions of Jacquin et al. [22]. Figure 4(a) illustrates the increase in fluctuation levels as α is increased and the appearance of a well marked peak when $\alpha > 3.0^o$ for $M = 0.75$. Similarly, figure 4(b) shows that the same peak arises when the Mach number is increased above the value 0.73 for $\alpha = 4^o$. Both an increase in Mach and angle of attack leads to an increase in the peak level and frequency, which is about $S_t = 0.07$, the same value as in Jacquin et al. [22]. These same trends were reported by Jacquin for the OAT15A airfoil, suggesting a weak dependence of the phenomenon upon the particular airfoil geometry.

The flow unsteadiness is associated with a large displacement of the shock wave, as can be observed in figure 5 which shows the two extreme positions of the shock wave using the Schlieren visualizations. The periodic movements of the shock are synchronized with a separation of the flow downstream of the shock. Flow separation is visible from the orientation of the black area present right behind the shock wave, which is oriented upward in figure 5(a) and downward, along the airfoil geometry, in figure 5(b). At the shock most upstream position, flow separation is present while at the most downstream location, the flow is attached to the wing. Three-dimensional effects also appear in the course of this evolution, possibly as a consequence of flow separation which is intimately a three-dimensional phenomenon or due to an intrinsic three-dimensional dynamics of the interacting shock wave.

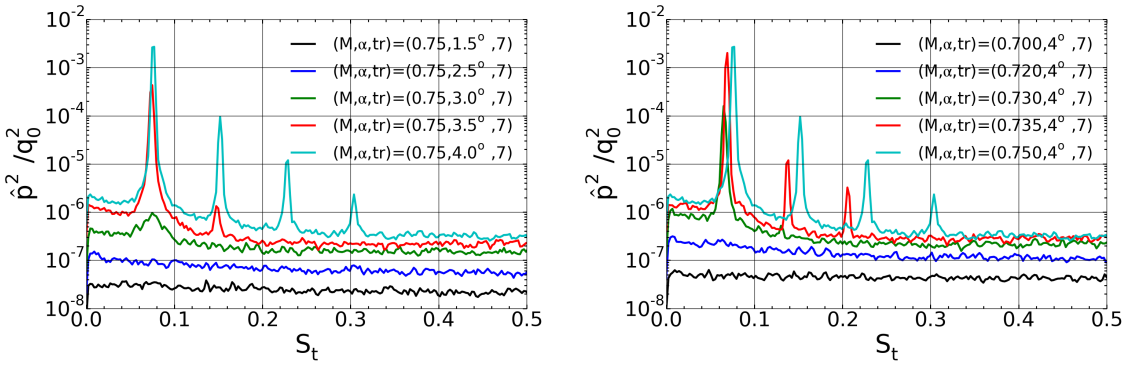

(a) (b)

Figure 4: Power Spectral Density of pressure normalized on free stream dynamic pressure q_0 at $x/c = 97\%$. Influence of (a) angle of attack when $M = 0.75$ and (b) Mach number when $\alpha = 4^o$ on the shock dynamics in the turbulent $tr = 7$ case.

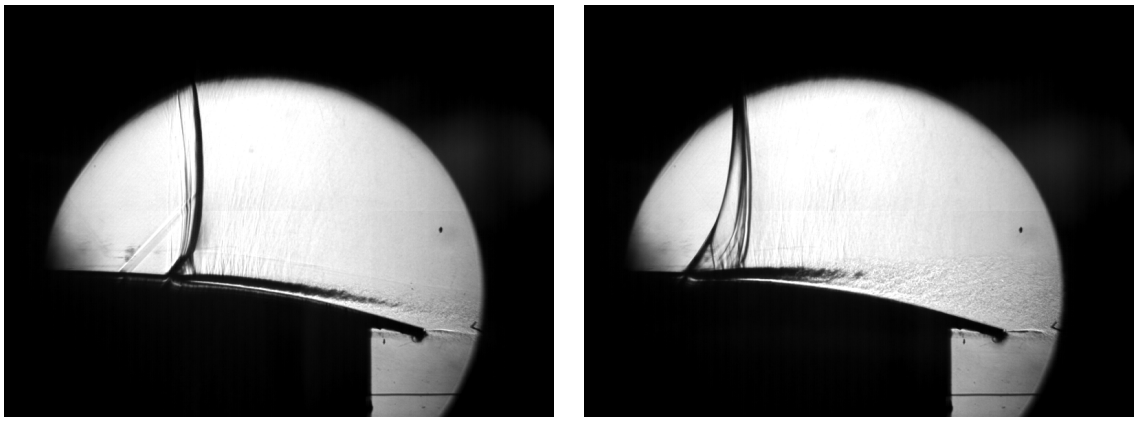

(a) (b)

Figure 5: Schlieren visualizations of the flow in the turbulent case $tr = 7$. Shock wave in (a) most upstream and (b) most downstream position.

3 Analysis and laminar results

3.1 Exploration of the laminar dynamics

A preliminary exploration of the laminar dynamics is obtained by removing the tripping tape from the previous turbulent situation. Figure 6 compares the previous turbulent $tr = 7$ and the now laminar $tr = 0$ cases in terms of pressure distribution and PSD for $(M, \alpha) = (0.735, 4^o)$. It is observed that the laminar case deviates significantly from the turbulent case. First the shock wave is located at a much more downstream location, shifting from approximately 50% of chord (on average) for $tr = 7$ to 60% of chord for $tr = 0$. The pressure plateau is also higher in the laminar case which indicates a stronger increase of the velocity at the upper surface. Finally the longitudinal extent of the slope of the pressure increase associated with the shock wave is steeper in the laminar case. This indicates that the shock exhibits weaker oscillations, since it is known that shock oscillations lead to a smearing of the shock signature in the pressure distribution.

Pressure PSD in figure 6(b) show that the flow also exhibits an unsteadiness in the laminar

case, with a dominant peak at a normalized frequency $S_t = 1.1$ which is to be compared to the value $S_t = 0.07$ associated with the turbulent case. Two harmonics of the main frequency peak are similarly observed in the two configurations (turbulent and laminar) and the primary peak levels are approximately equal. In addition to the main peak, a low frequency bump is also apparent in the laminar case at about $S_t = 0.05$.

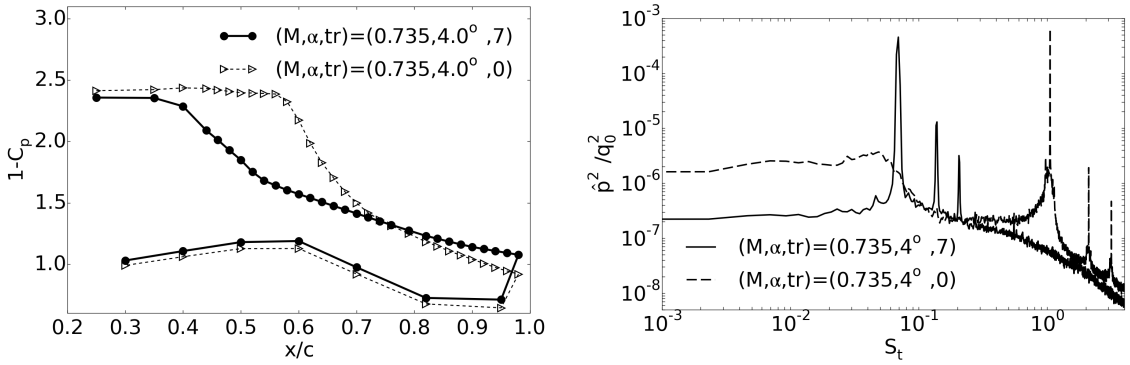

(a) (b)

Figure 6: Comparison between turbulent $tr = 7$ and laminar $tr = 0$ configurations. (a) Chord-wise time averaged pressure distributions. (b) PSD of the pressure signals in the laminar and turbulence cases, sensor location being $x/c = 73\%$.

A Fourier analysis of the Schlieren images $I(x, z, t)$ in the laminar $tr = 0$ case reveals the same two dominant unsteady modes that were captured by the pressure spectra. Figure 7 shows the Power Spectral Density of $|\hat{I}|(x, z, f)$ for the low and high frequency modes, that is $S_t = 0.05$ and $S_t = 1.1$, and the PSD as function of normalized frequency considering the maximum PSD intensity at each frequency. This spectrum exhibits the low frequency mode, and the high frequency mode, with its first harmonics. The low frequency mode is distributed along the shock wave and corresponds to a low frequency oscillations of the shock wave in the chordwise direction. The oscillations of the shock induced by this mode, typically on the order of 5% of chord, are well observed when the Schlieren snapshots are animated (not shown). The high frequency mode shows that the dominant mode affects the bottom part of the shock wave, and features an upward travelling wave along the shock, which can be guessed from the two vertically aligned lobes that are present on top of it.

Overall this preliminary comparison of the turbulent and laminar dynamics establishes that laminarity strongly affects the aerodynamics of the airfoil, in terms of forces as is apparent from the difference in pressure distributions and in terms of flow dynamics as the laminar case introduces a reduced low frequency mode and a dominant high frequency mode, the latter being not present in the turbulent case. This shift in the dynamics is associated with a much smaller extension of the shock movement in the chordwise direction and an intense dynamics of the shock foot. The dominant modes of the laminar setting at $M = 0.735$ are at $S_t = 0.05$ and $S_t = 1.1$, which must be compared to the turbulent $tr = 7$ case which features $S_t = 0.07$. The low frequency dynamics of the laminar case resembles that of the turbulent case, although the shock movement is much weaker and involves a wider range of frequencies.

3.2 Effect of Mach number and angle of attack

In this section the variations of the laminar flow with M and α are presented. Figure 8 shows the effect of angle of attack and Mach number on the evolution of time averaged pressure along the airfoil in the laminar $tr = 0$ case. In figure 8(a) the angle of attack is varied from 1.5^o to 4^o at

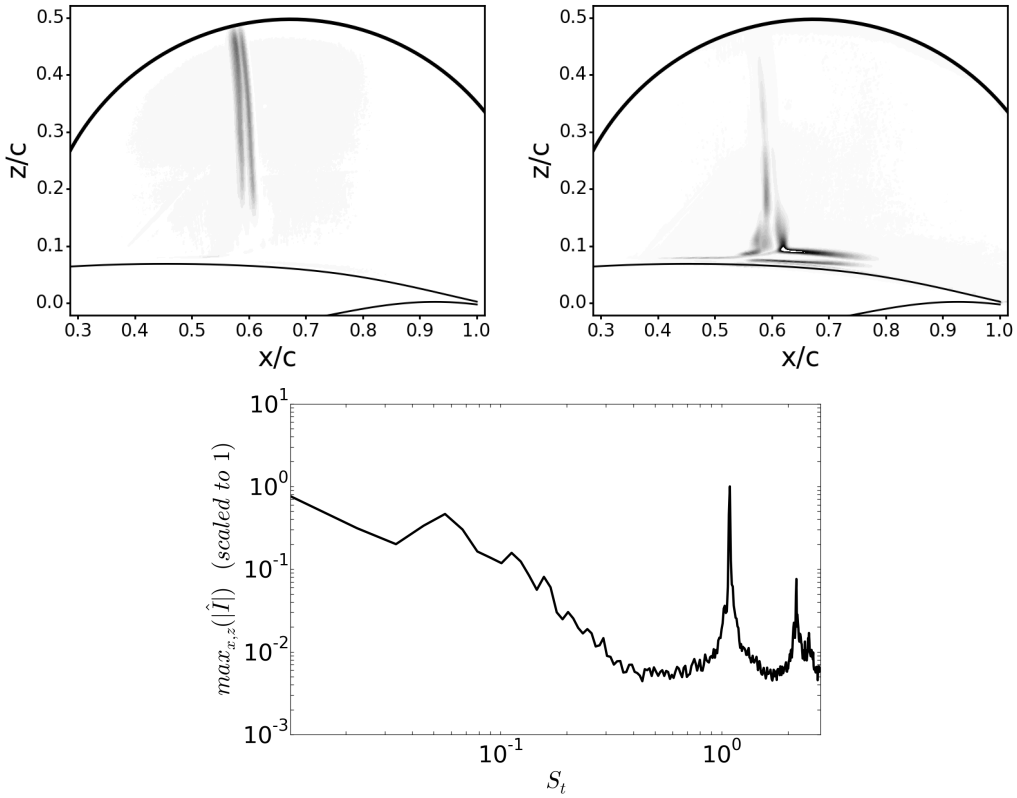

Figure 7: Fourier analysis of the recording of the Schlieren visualizations showing in (top left) the PSD mode at $S_t = 0.05$, in (top right) the PSD mode at $S_t = 1.1$ and in (bottom) the PSD of Schlieren image intensity, considering maximum intensity at each frequency $max_{x,z}|\hat{I}|$ (and scaled to one) as a function of normalized frequency. The airfoil contour is shown in the top frames for clarity.

$M = 0.735$. As α increases the flow at the suction side accelerates more. This strengthens the shock wave and pushes it further downstream. In fact only a weak variation of the shock location is observed above $\alpha = 2.5^o$, with the maximum value being about 60% of chord. The region ahead of the shock exhibits a plateau which corresponds to the rather flat geometry of the first half of the suction surface (see figure 2). Above $\alpha = 3.5^o$ the shock starts to spread in the streamwise direction and flow separation is apparent at the trailing edge as the mean C_p moves away from the value adopted at lower incidences.

The increase in Mach number evaluated by figure 8(b), for $\alpha = 4^o$, shows that as M rises the shock is moved downstream but only weakly strengthened. The shock position locks at the 60% position reported previously above $M = 0.73$ and starts to spread as the Mach is further increased. For this incidence of 4^o the increase in Mach number causes a lower plateau level ahead of the shock which indicates that lift is being reduced. This agrees with the flow separation that is evidenced by the increase in C_p level at the trailing edge for the highest Mach number value.

The effect of Mach number and angle of attack on the shock dynamics is illustrated in the PSD of pressure plotted in figure 9 with the pressure delivered by the sensor located at $x/c = 97\%$. It appears that an increase in M or α leads to a reduction of the frequency of the high frequency mode. This is opposite to the turbulent case and in agreement with the results obtained by Finke [18].

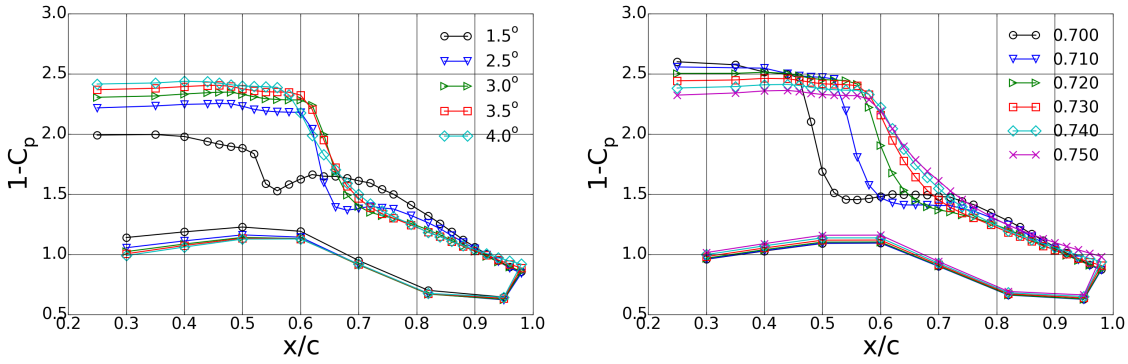

(a) (b)

Figure 8: Time averaged pressure distribution for the laminar $tr = 0$ case. Effect of (a) angle of attack for $M = 0.735$ and (b) Mach number for $\alpha = 4^o$.

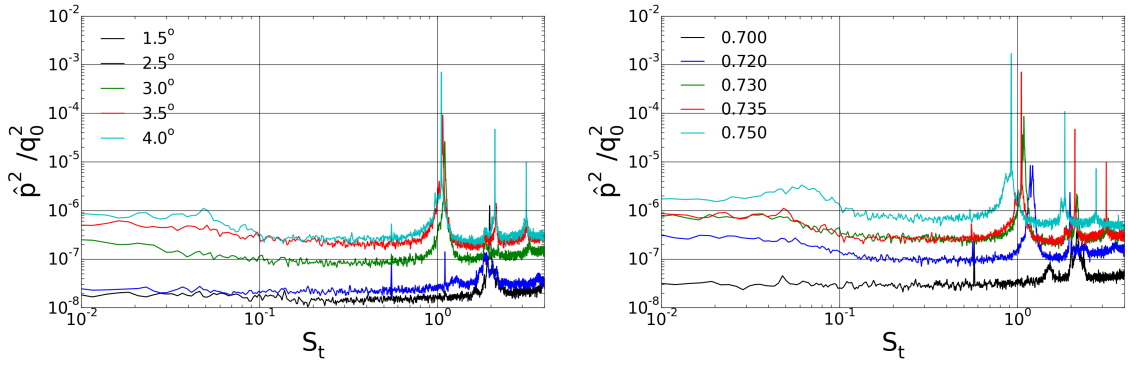

(a) (b)

Figure 9: Power Spectral Density of pressure fluctuations at the location $x/c = 97\%$. Effect of (a) angle of attack for $M = 0.735$ and (b) Mach number for $\alpha = 4^o$.

In figure 9(b) the low frequency peak can be observed for $M = 0.75$. Figure 10 shows more specifically the evolution of this low frequency peak as a function of angle of attack and Mach number. The low frequency peak is seen to increase in amplitude and frequency as either M or α are increased. It must be noted that this matches the behavior of the turbulent buffet phenomenon described by Jacquin et al. [22] and the results of Finke [18]. Lastly figure 9 and figure 10 show that the low frequency peak arises at larger values of α and M than the high frequency mode.

3.3 Laminar separation bubble

Figure 11 shows the evolution of the mean pressure coefficient along the suction surface when C_p is referenced about the value C_{p0} taken at $x/c = 30\%$ in the plateau region where pressure levels vary little and the x coordinate is offset with respect to the mean location of the shock wave x_{shock}. The latter is approximated as the location of the chord-wise maximum of the time averaged pressure variations. This particular choice allows to automatically locate the shock wave in the data. The data is shown for the turbulent $tr = 7$ and laminar $tr = 0$ cases and highlights two important features of the laminar case. The first one is the presence of a pressure rise ahead of the shock wave which is absent in the turbulent case. From literature (see Schlichting [41]) it appears that this

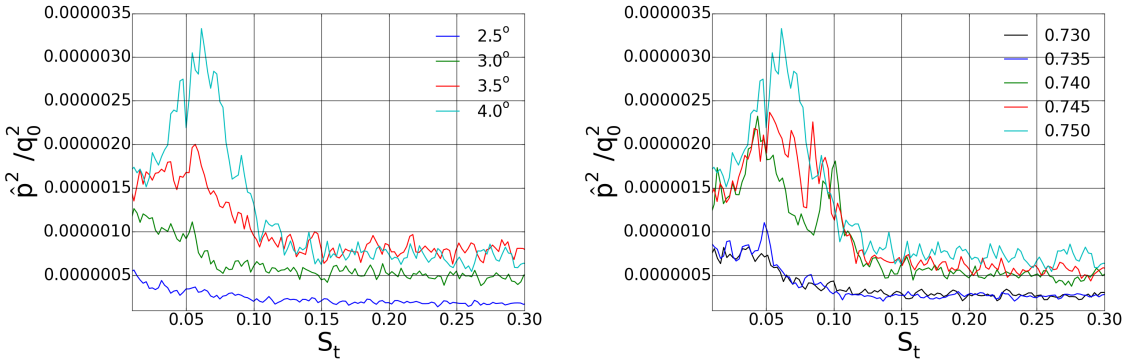

(a) (b)

Figure 10: Power Spectral Density of pressure fluctuations at $x/c = 97\%$. Zoom in the low frequency domain and analysis of the effect of (a) angle of attack at $M = 0.75$ and (b) Mach number at $\alpha = 4^o$.

behavior is typical of a laminar separation in a supersonic flow. This pressure rise is followed by a pressure plateau prior to the strong compression associated with the shock wave. The behavior of the flow in such a circumstance is described by the free interaction theory by means of empirical correlations, see for instance Babinsky and Harvey [3]. Figure 11(b) shows that the pressure curves feature all this pre-compression pattern. Therefore it appears that the laminar separation is present for all the Mach numbers investigated.

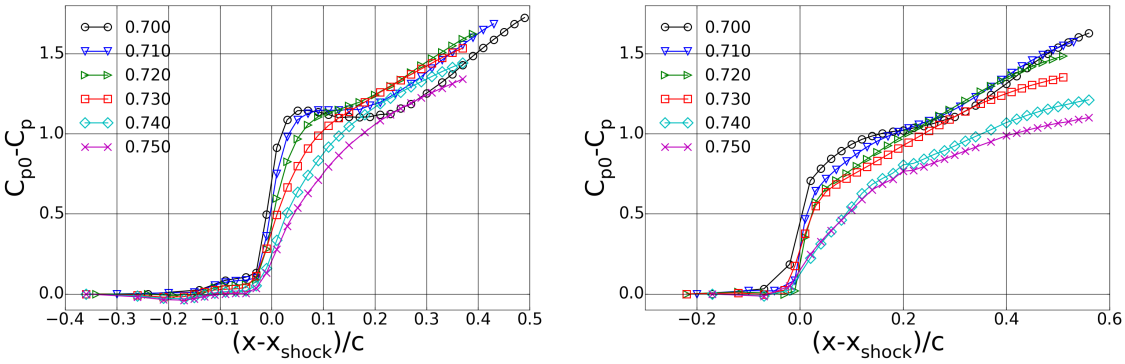

(a) (b)

Figure 11: Evolution of the time averaged pressure in the regon of the shock. Analysis of the effect of increasing Mach number for the (a) turbulent and (b) laminar case. The x coordinates is referenced to the position of the shock x_{shock}, taken here as the location of maximum variation in the time averaged pressure. The pressure coefficient is referenced about the pressure coefficient C_{p0} taken at $x/c = 30\%$.

A close-up view of the region where pressure starts to rise is displayed in figure 12. In this figure, pressure is normalized on the minimum pressure p_{min} that occurs ahead of the shock wave and not on free stream properties like in figure 11(b) while axial distance remains referenced about the mean shock location x_{shock}. This makes the curves start all from the same level ahead of the laminar separation and the curve nicely arrange on top of one another in the plot. It allows then to compare the current setup with the free interaction theory that predicts that the level of pressure in the plateau region $p_{plateau}$ increases with the skin friction coefficient at separation and

decreases with the Mach number outside the boundary layer. The main effect is expected to be that of the Mach number, the position of the shock wave and the Reynolds number, that scale the friction coefficient, varying little in the current configuration. The decrease of the pressure level in the plateau in figure 12 as the upstream Mach number increases therefore agrees with the free interaction theory, which reinforces the claim that the laminar separation in the current flow is similar to the pattern generally found in laminar shock wave boundary layer interactions.

The second feature to be observed in figure 11 is that the pressure increase due to the shock is larger in the laminar than in the turbulent case. This is to be related to the more downstream location of the shock in the laminar case, as seen in figure 6. An important consequence of the increased shock strength in the laminar case is that it should lead to higher wave drag and thus could penalize the benefit of the laminar stream passing by the airfoil. This consequence is important to bear in mind in case a practical application of such a system were to be attempted.

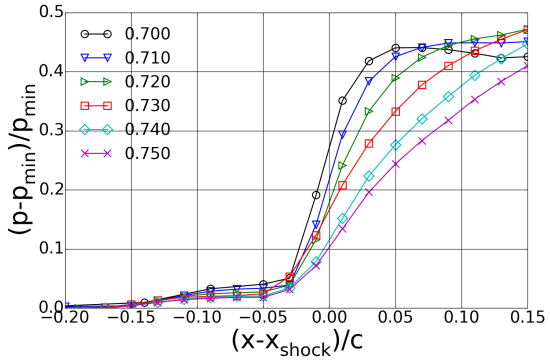

Figure 12: Same as figure 11(b) but with the pressure referenced to the minimum pressure p_{min} in the plateau region before the laminar separation, and normalized upon p_{min}.

3.4 Laminar separation bubble

In this section we detail visualizations of the laminar separation bubble that were made using condensed humidity as a flow tracer. The process goes as follows. Without input of dry air into the wind tunnel flow stream, flow acceleration at the body surface and the associated temperature decrease can lead to condensation and formation of water droplets. In the present analysis this was implemented by turning off the humidity control of the wind tunnel. A laser illumination (identical to the one used for Particle Image Velocimetry), flashing at 4Hz, of a plane aligned with the flow and vertical above the top surface of the airfoil was then used to visualize the behavior of these water droplets. Figure 13 shows a zoom of the flow close to the suction side in the laminar separation region. What is seen are the water droplets passing above the surface and leaving a dark region free of any seeding right above the surface. Unlike previous tests, in these flow experiments with condensed water the surface of the wing is not painted and the smooth metal surface plays the role of a mirror. This explains why the image appears symmetric. Therefore only the top part is of interest, and the curve delineating the symmetry axis is in fact the top surface of the airfoil.

The height of the separation is on the order of $1mm$. Attemps to qualify it using PIV were ruined by the intense light reflections at the wall, which could not be sufficiently removed and prevented any measurements in the bubble region. The current method with natural seeding proved to be free of these reflections and to allow for the visualization of the bubble separating streamline, thanks to the important contrast between the recirculation region without droplets and the region above, filled with droplets. It is thought that this contrast is also helped by the rather larger size of these

droplets compared to PIV seeding, which allows intense scattering of the laser light. A side effect is that the inertia of these particles being more pronounced their use as tracers may be affected. However owing to the mostly longitudinal motion of the flow in the region of interest, and the fact that the gradient imposed by the shock is almost normal to the particles trajectories, this effect does not seem detrimental to observe the separating streamline of the bubble.

The absence of seeding in the laminar separation bubble is a well known phenomenon (see Giepman et al. [19]) and seems to be the consequence of the low diffusion rate of particles at the interface of the bubble in the laminar regime. In the present case, one has also to consider the condensation process to explain why condensation occurs in the upstream boundary layer and not in the bubble. For a stationary bubble, and from a general perspective, the mechanism could be that the recirculating fluid gets warmer due to its friction at the wall and its persistence in the bubble, which prevents the condensation of humidity, contrary to the external flow which is persistently fed by humid and cold (due to the flow acceleration at the airfoil suction side) air. In the unsteady case, it is known (see for instance Piponniau et al. [35]) that the bubble exchanges fluid with the above flow. However, this occurs at the rear of the bubble where the fluid is also warmer and characterized by a lower concentration of particles due to turbulent diffusion. It thus appears from this analysis that the droplets physically remain above the separating streamline at the fore part of the bubble and that the separation between the seeded and the unseeded zones can be used to delineate the locus of this separating streamline.

To analyze the behavior of the bubble figure 13 hence shows a sequence of this naturally seeded flow passing above the bubble. This sequence shows several realizations of the bubble separating streamline, that are uncorrelated since laser flashes at 4Hz. One can observe the separation of the boundary layer at the left, the development of the separated flow, with the recirculation below and the external flow above, and the development of turbulence through the action of the Kelvin-Helmholtz (KH) instability. The latter is evidenced by the wavy deformations of the separating streamline at the top of the recirculation region and the formation of large scale eddies. This sequence suggests that one of the mechanism of the high frequency peak may be the destabilization of the laminar separation bubble.

3.5 Effect of surface roughness

Surface roughness has been sampled at several locations on the wing upper and lower surfaces with and without paint. The surface roughness measuring instrument is the Mitutoyo Surftest SJ-301 instrument that scans over a length of 4mm at a speed of 0.5mm/s and delivers as roughness parameters the arithmetical mean Ra, the root mean square Rq and the average distance between a selection of highest peaks and lowest valleys Rz according to the Japanese Industrial Standard JIS2001. Table 2 indicates the results averaged over the ensemble of sampling locations for the different roughness situations. In particular the case with paint comprises a preliminary raw configuration that was found to generate an early transition of the boundary layer and was then sandpapered to reduce roughness. This successfully allowed the laminar state up to the shock wave. Generally the table indicates that a Ra value larger than roughly $2\mu m$ leads to the transition of the boundary layer upstream of the shock wave. In details the investigation does not allow to differentiate the effects of mean and maximum roughness but gives indication on the typical level of roughness needed to allow the laminar boundary layer for the current setting and Reynolds number, i.e. $Ra, Rq = 0.1 - 1\mu m$ and $Rz < 10\mu m$.

It was further discovered that the presence of paint modifies the frequency of the shock unsteadiness as is illustrated in figure 14. This figure shows the case with paint and several cases without paint. The noticeable change is that the frequency of the high frequency peak without paint is lower than with paint. The influence of Mach number is retained (frequency decreases as Mach increases). Several works (see Agostini et al. [2], Piponniau et al. [35] or Larcheveque et al. [25]) show that the frequency of the dynamics of a shock wave boundary layer interaction in presence of a mean

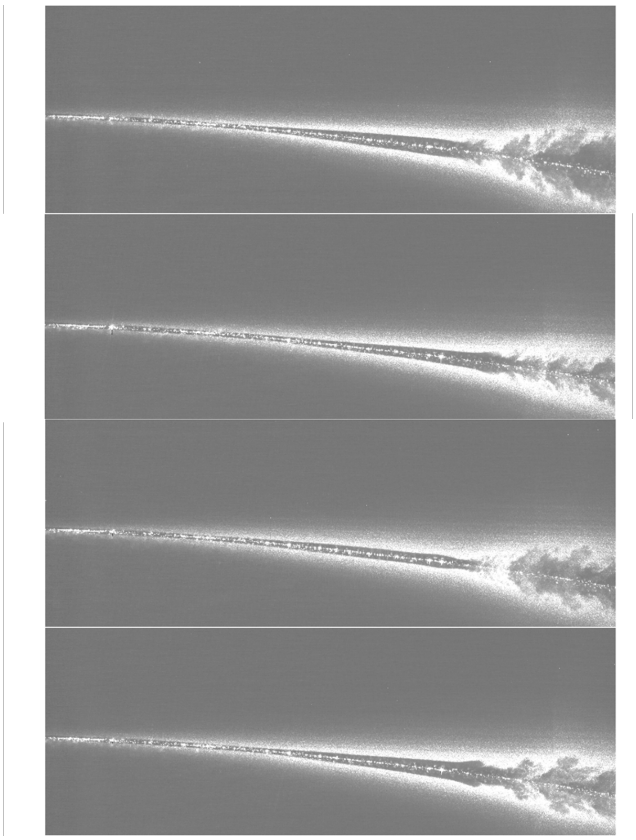

Figure 13: Laminar separation bubble visualized using naturally forming water droplets and laser flashes. The flow is for $(M, \alpha, tr) = (0.735, 4^o, 0)$ and exhibits the high frequency peak.

separation at the shock foot scales on the bubble length. In the present situation the additional roughnesses with the paint introduce extra perturbations upstream of the laminar separation that are expected to drive a faster establishment of turbulence in the interaction and thus a more rapid reattachment of the flow. The bubble must accordingly be smaller and the associated frequency, which following this theory, would scale as the inverse of this distance, to be higher, as is observed.

4 Flow control

Two control strategies have been tested to increase the stability of the flow: three-dimensional bumps and steady jets. These devices have been developped in a separate and preliminary investigation that is not described here. The design of the bumps and jets is schematized in figure 15.

The jet configuration has been designed for the test case $(M, \alpha, tr) = (0.74, 4^o, 0)$. The jets are located at 56.5% of chord slightly upstream of the shock wave which is at 60% of chord. Jets are oriented at pitch and toe angle of 30 and 90 degrees respectively. This inclination of the jets about the stream above the surface of the wing causes the generation of longitudinal vortices, the effect of which tends to reduce flow separation behind the shock, as was previously observed for the control of flow separation on a three-dimensional wing in the transonic regime, see Molton et al. [33]. The jet device comprises 75 jets uniformely distributed along the span, at intervals equal

Parameter	w/o paint	w/ paint (raw)	w/ paint (sandpapered)
Ra (μm)	0.3	2.4	1.6
Rq (μm)	0.4	3.1	2.0
Rz (μm)	1.75	14.7	9.0
laminar/turbulent	laminar	turbulent	laminar

Table 2: Surface roughness parameters with and without paint and indication of the state of the boundary layer developing on the upper surface.

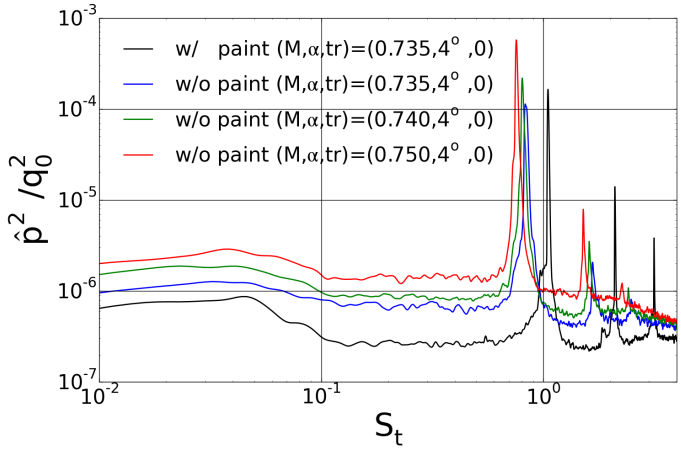

Figure 14: Power Spectral Density of the pressure fluctuations taken at $x/c = 97\%$. Influence of the paint compared to the unpainted case. The unpainted case comprises several Mach numbers to validate that the same Mach influence (decrease of peak frequency with Mach number) is obtained with and without paint.

to $\lambda_j = 20d_j = 10mm$ where $d_j = 0.5mm$ is the jet diameter.

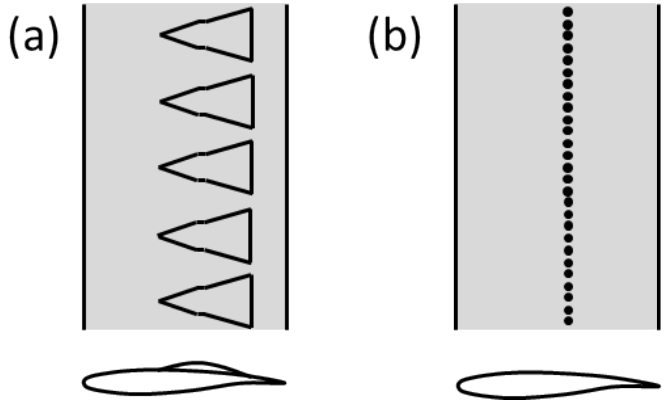

Figure 15: Schematics of the control devices. (a) three-dimensional bumps and (b) steady jets. Top row : top view. Bottom row : airfoil section view.

Bumps have been originally introduced as a method to control transonic flows in order to reduce wave drag, see Ashill et al. [9]. While wave drag at design conditions is usually minimized it strongly

increases at off-design conditions when either Mach number or angle of attack is increased. This transonic drag rise can be efficiently controlled with such bumps, that contour the airfoil in order to deflect the supersonic flow at the suction side and generate oblique shock waves ahead of the main straight shock, which creates a more isentropic transformation. Colliss et al. [10] and Bogdansky et al. [7] showed that three-dimensional, finite-span bumps, on top of reducing wave drag, can also be advantageous to postpone buffet. The yet to be confirmed mechanism [7, 17, 9] would lie in the formation of longitudinal vorticity at the side flanks of the three-dimensional bumps, which help preventing the flow from separating behind the shock wave.

In the present setting the bump device comprises 11 bumps uniformely distributed along the span. Each bump features a wedge shape growing in width from the bump leading edge located at 46.2% of chord to the bump trailing edge located at 80% of chord. Maximum bump height is reached at the crest at the middle of the bump and equals 0.28% of chord, i.e. 6.44mm. The crest is 10% of chord wide and 3% of chord long, and starts 17% of chord from the bump leading edge. The bump trailing edge is 21.2% of chord wide.

4.1 Three-dimensional bumps

Figure 16 shows the pressure distribution about the airfoil with the bump installed compared to the baseline (smooth) case. With the bumps, pressure was sampled along two separate lines, one at a spanwise location corresponding to the bump leading edge and another one in-between two bumps. It is observed that the bump slightly reduces shock strength, as is evidenced from the departure of the pressure distribution at the bump line compared to baseline and to the data taken in between two bumps.

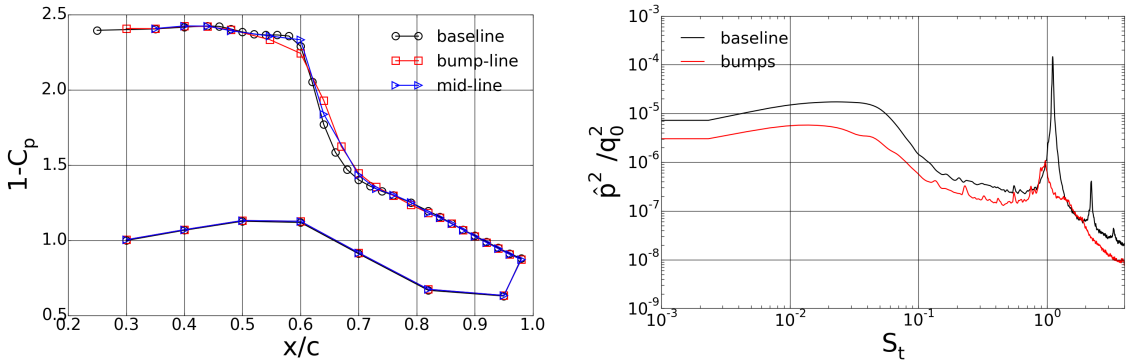

(a) (b)

Figure 16: Effect of the bumps on (a) the time averaged pressure distribution along the airfoil and (b) Power Spectral Density of pressure fluctuations at $x/c = 64\%$. The flow case is $(M, \alpha, tr) = (0.73, 3.5^o, 0)$.

Regarding flow unsteadiness, figure 16(b) shows that a reduction in intensity of the high frequency peak is achieved. Yet the flow unsteadiness is not fully suppressed. This reduction of the unsteadiness seems to validate the scenario following which three-dimensional bumps generate axial vorticity which is able to limit flow separation behind the shock wave. However these vortices are apparently not strong enough to fully control flow separation and cancel buffet.

4.2 Steady jets

The strength of the jets is controlled using the jet momentum coefficient given by

$$C_\mu = \frac{\rho_j U_j^2 S_j}{0.5 \rho U_0^2 S_{ref}} \tag{2}$$

where S_{ref} is the reference surface taken here as the surface of the wing $S_{ref} = s \times c$, U_0 is the velocity of the freestream and ρ the specific mass of the air in the test section, U_j is the velocity of the jets obtained by assuming an isentropic transformation between plenum and outside, ρ_j the specific mass of air in the jet and S_j the surface of the holes that form the jets. The value of C_μ is obtained from the total mass flow rate going through the jets, which is the parameter which is measured and controlled during the tests. Mass flow rates from 0 to 9.5g/s have been tested, which yield C_μ values from 0 to 0.075%.

Figure 17(a) shows the modification of the pressure distribution when the jets are activated. For sufficient momentum coefficient, $C_\mu > 0.065\%$, the pressure map is clearly modified and an increased lift is achieved. From the PSD of pressure shown in figure 17(b), it can be observed that the jets are able to fully stabilize the flow. Indeed the high frequency peak is completely suppressed from the dynamics.

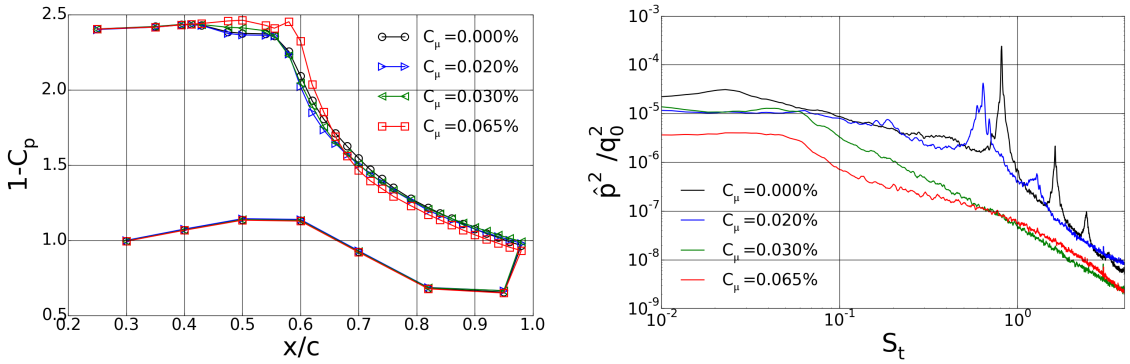

(a) (b)

Figure 17: Influence of C_μ with, in (a), the time averaged pressure distribution and in (b) Power Spectral Density of pressure fluctuations. Laminar flow case $(M, \alpha, tr) = (0.735, 4^o, 0)$.

The jets were also tested in the turbulent $tr = 7$ case and the results are shown in figure 18. In the turbulent case when buffet occurs, the jets lie behind the mean position of the shock wave which is at about 50% of chord. Figure 18(a) shows the pressure distribution without and with control. It is observed that a significant increase in lift is also achieved with the control in the turbulent case. This is related to the suppression of the buffet phenomenon, as can be observed in figure 18(b) where the low frequency peak of the turbulent buffet phenomenon has disappeared thanks to the jet blowing. Therefore the jets are also successful to stabilize the flow in the turbulent situation.

5 Conclusion

An experimental investigation of the transonic flow past a laminar wing has been accomplished in order to investigate the effect of laminar flow on the buffet phenomenon. Results reveal the existence of a critical phenomenon peculiar to the laminar case which occurs at a frequency about $S_t = 1.1$, in sharp contrast with the turbulent buffet phenomenon which occurs at a frequency close

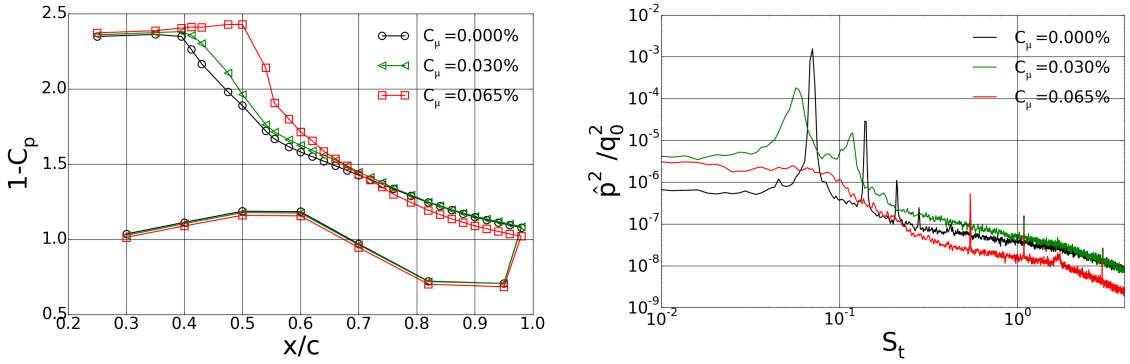

(a) (b)

Figure 18: Influence of C_μ with, in (a), the time averaged pressure distribution and in (b) the Power Spectral Density of pressure fluctuations. Turbulent flow case $(M, \alpha, tr) = (0.735, 4^o, 7)$.

$S_t = 0.07$. A similar low frequency dynamics is also shown to exist in the laminar case, yet at a slightly lower frequency $S_t = 0.05$. These low and high frequency modes look similar to those found by Finke [18] in particular the evolution of their frequency with Mach and angle of attack are consistent with Finke's results. However the frequency of the high frequency peak is notably higher in the present case. It is difficult to say at this stage whether this is due to the different airfoil geometry or if these are two different dynamics. It appears though that both are related to the bubble dynamics.

An interesting feature is that the shock is stronger in the laminar configuration than in the turbulent one. Wave drag will hence certainly be higher in the laminar case. This means that the use of laminar flows to reduce drag requires to take into account all the components of drag, not only the benefit of reduced skin friction, to analyze the overall drag reduction.

Finally flow control has been tested in order to reduce the oscillations of the flow caused by the high frequency peak, using two different control strategies, bumps and steady jet blowing. It is shown that bumps are able to reduce the intensity of the laminar buffet phenomenon. Jets appear as the most efficient technique as they allow a full stabilization of the flow in both the laminar and turbulent cases.

Acknowledgements

This work has been supported by the European FP7 Project BUTERFLI (FP7-AAT-2013.8-1-RTDRUSSIA) program. The authors would like to thank all the people who dedicated much of their time to make this experiment possible, in particular Jean-Pierre Tobeli, Jean-Charles Abart, Paul Paillart, François Lambert, Philippe Geffroy, Michel Vegran, Thierry Pot and Pascal Audo.

References

[1] Buffet and transition delay control investigated with european-russian cooperation for improved flight performance. final report. https://cordis.europa.eu/docs/results/605/605605/final1-buterfli-final-report-complete-report.pdf. Accessed: 2018-10-23.

[2] L. Agostini, L. Larchevêque, and P. Dupont. Mechanism of shock unsteadiness in separated shock/boundary-layer interactions. *Physics of Fluids*, 27(12):126103, 2015.

[3] H. Babinsky and J.K. Harvey. *Shock wave-boundary-layer interactions*, volume 32. Cambridge University Press, 2011.

[4] G. Barakos and D. Drikakis. Numerical simulation of transonic buffet flows using various turbulence closures. *International Journal of Heat and Fluid Flow*, 21(5):620–626, 2000.

[5] R. E. Bartels. Computation of shock buffet onset for conventional and supercritical airfoil. In *35th AIAA Aerospace Sciences Meeting and Exhibit*, number 97-0833, 1997.

[6] R.E. Bartels. Flow and turbulence modeling and computation of shock buffet onset for conventional and supercritical airfoils. 1998.

[7] S. Bogdanski, K. Nübler, T. Lutz, and E. Krämer. Numerical investigation of the influence of shock control bumps on the buffet characteristics of a transonic airfoil. In *New Results in Numerical and Experimental Fluid Mechanics IX*, pages 23–32. Springer, 2014.

[8] V. Brion, J. Dandois, J.-C. Abart, and P. Paillart. Experimental analysis of the shock dynamics on a transonic laminar airfoil. *Progress in Flight Physics–Volume 9*, 9:365–386, 2017.

[9] P.J.K. Bruce and S.P. Colliss. Review of research into shock control bumps. *Shock Waves*, 25(5):451–471, 2015.

[10] S.P. Colliss, H. Babinsky, K. Nübler, and T. Lutz. Vortical structures on three-dimensional shock control bumps. *AIAA Journal*, pages 2338–2350, 2016.

[11] E.S. Cornette. Wind-tunnel investigation of the effects of wing bodies, fences, flaps, and a fuselage addition on the wing buffet response of a transonic-transport model. 1961.

[12] J.D. Crouch, A. Garbaruk, D. Magidov, and A. Travin. Origin of transonic buffet on aerofoils. *Journal of Fluid Mechanics*, 628:357–369, 2009.

[13] J. Dandois. Experimental study of transonic buffet phenomenon on a 3d swept wing. *Physics of Fluids*, 28(1):016101, 2016.

[14] Julien Dandois, Ivan Mary, and Vincent Brion. Large-eddy simulation of laminar transonic buffet. *Journal of Fluid Mechanics*, 850:156–178, 2018.

[15] S. Deck. Numerical simulation of transonic buffet over a supercritical airfoil. *AIAA journal*, 43(7):1556–1566, 2005.

[16] J.B. Dor, A. Mignosi, A. Seraudie, and B. Benoit. Wind tunnel studies of natural shock wave separation instabilities for transonic airfoil tests. In *Symposium Transsonicum III*, pages 417–427. Springer, 1989.

[17] J.P. Eastwood and J.P. Jarrett. Toward designing with three-dimensional bumps for lift/drag improvement and buffet alleviation. *AIAA journal*, 50(12):2882–2898, 2012.

[18] K Finke. Shock oscillations in transonic flows and their prevention. In *Symposium Transsonicum II, Göttingen, September 8-13, 1975*, page 57. Not Avail, 1976.

[19] RHM Giepman, FFJ Schrijer, and BW Van Oudheusden. High-resolution piv measurements of a transitional shock wave–boundary layer interaction. *Experiments in Fluids*, 56(6):113, 2015.

[20] A. Hartmann, A. Feldhusen, and W. Schröder. On the interaction of shock waves and sound waves in transonic buffet flow. *Physics of Fluids*, 25(2):026101, 2013.

[21] A. Hartmann, M. Klaas, and W. Schröder. Time-resolved stereo piv measurements of shock–boundary layer interaction on a supercritical airfoil. *Experiments in fluids*, 52(3):591–604, 2012.

[22] L. Jacquin, P. Molton, S. Deck, B. Maury, and D. Soulevant. Experimental study of shock oscillation over a transonic supercritical profile. *AIAA journal*, 47(9):1985–1994, 2009.

[23] H. John. Critical review of methods to predict the buffet capability of aircraft. Technical report, DTIC Document, 1974.

[24] L.-E. Jones, R.-D. Sandberg, and N.-D. Sandham. Direct numerical simulations of forced and unforced separation bubbles on an airfoil at incidence. *Journal of Fluid Mechanics*, 602:175–207, 2008.

[25] L. Larchevêque. Low–and medium–frequency unsteadinesses in a transitional shock–boundary reflection with separation. In *54th AIAA Aerospace Sciences Meeting*, page 1833, 2016.

[26] B.H.K. Lee. Self-sustained shock oscillations on airfoils at transonic speeds. *Progress in Aerospace Sciences*, 37(2):147–196, 2001.

[27] B.H.K. Lee and F.C. Tang. Transonic buffet of a supercritical airfoil with trailing-edge flap. *Journal of Aircraft*, 26(5):459–464, 1989.

[28] H.W. Liepmann. The interaction between boundary layer and shock waves in transonic flow. *Journal of the Aeronautical Sciences*, 2012.

[29] D.G. Mabey. Buffeting criteria for a systematic series of wings. *Journal of Aircraft*, 26(6):576–582, 1989.

[30] LM Mack. Special course on stability and transition of laminar flow. *AGARD report*, 709, 1984.

[31] J. B. McDevitt and A. F. Okuno. *Static and dynamic pressure measurements on a NACA 0012 airfoil in the Ames high Reynolds number facility*, volume 2485. National Aeronautics and Space Administration, Scientific and Technical Information Branch, 1985.

[32] W. Merzkirch. *Flow visualization*. Elsevier, 2012.

[33] P. Molton, J. Dandois, A. Lepage, V. Brunet, and R. Bur. Control of buffet phenomenon on a transonic swept wing. *AIAA journal*, 51(4):761–772, 2013.

[34] E. Obert. *Aerodynamic design of transport aircraft*. IOS press, 2009.

[35] S. Piponniau, J.P. Dussauge, J.F. Debieve, and P. Dupont. A simple model for low-frequency unsteadiness in shock-induced separation. *Journal of Fluid Mechanics*, 629:87–108, 2009.

[36] E.J. Ray and R.T. Taylor. Buffet and static aerodynamic characteristics of a systematic series of wings determined from a subsonic wind-tunnel study. 1970.

[37] T.A. Reyhner and I. Flügge-Lotz. The interaction of a shock wave with a laminar boundary layer. *International Journal of Non-Linear Mechanics*, 3(2):173–199, 1968.

[38] F. Sartor, C. Mettot, and D. Sipp. Stability, receptivity, and sensitivity analyses of buffeting transonic flow over a profile. *AIAA Journal*, 53(7):1980–1993, 2014.

[39] F. Sartor and S. Timme. Delayed detached–eddy simulation of shock buffet on half wing–body configuration. *AIAA Journal*, pages 1–11, 2016.

[40] H. Schlichting and K. Gersten. *Boundary-layer theory*. Springer Science & Business Media, 2000.

[41] H. Schlichting, K. Gersten, E. Krause, H. Oertel, and K. Mayes. *Boundary-layer theory*, volume 7. Springer, 1960.

[42] G.S. Settles. *Schlieren and shadowgraph techniques: visualizing phenomena in transparent media*. Springer Science & Business Media, 2012.

[43] Ante Soda. *Numerical investigation of unsteady transonic shock/boundary-layer interaction for aeronautical applications*. PhD thesis, RWTH Aachen, 2007.

[44] Q. Xiao, H. Tsai, and F. Liu. Numerical study of transonic buffet on a supercritical airfoil. *AIAA journal*, 44(3):620–628, 2006.